



Strongly Lensed Supernova Refsdal: Refining Time Delays Based on the Supernova Explosion Models

Petr Baklanov^{1,2,3} , Natalia Lyskova^{2,4} , Sergei Blinnikov^{1,5} , and Ken'ichi Nomoto⁵ 

¹NRC “Kurchatov Institute” - ITEP 117218 Moscow, Russia; petr.baklanov@itep.ru

²Space Research Institute (IKI), Russian Academy of Sciences, Profsoyuznaya 84/32, 117997 Moscow, Russia

³National Research Nuclear University MEPhI, Kashirskoe sh. 31, Moscow 115409, Russia

⁴P.N. Lebedev Physical Institute, Leninskiy prospect 53, Moscow 119991, Russia

⁵Kavli Institute for the Physics and Mathematics of the Universe (WPI), The University of Tokyo, Kashiwa, Chiba 277-8583, Japan

Received 2020 July 4; revised 2020 November 19; accepted 2020 November 23; published 2021 January 25

Abstract

We explore the properties of supernova (SN) “Refsdal”—the first discovered gravitationally lensed SN with multiple images. A large magnification provided by the galactic-scale lens, augmented by the cluster lens, gave us a unique opportunity to perform a detailed modeling of a distant SN at $z \simeq 1.5$. We present results of radiation hydrodynamics modeling of SN Refsdal. According to our calculations, the SN Refsdal progenitor is likely to be a more massive and energetic version of SN 1987A, i.e., a blue supergiant star with the following parameters: the progenitor radius $R_0 = (50 \pm 1)R_\odot$, the total mass $M_{\text{tot}} = (25 \pm 2)M_\odot$, the radioactive ^{56}Ni mass $M_{^{56}\text{Ni}} = (0.26 \pm 0.05)M_\odot$, and the total energy release $E_{\text{burst}} = (4.7 \pm 0.8) \times 10^{51}$ erg. Reconstruction of SN light curves allowed us to obtain time delays and magnifications for the images S2–S4 relative to S1 with higher accuracy than previous template-based estimates of Rodney et al. (2016). The measured time delays are $\Delta t_{\text{S2-S1}} = 9.5_{-2.7}^{+2.6}$ days, $\Delta t_{\text{S3-S1}} = 4.2_{-2.3}^{+2.3}$ days, and $\Delta t_{\text{S4-S1}} = 30_{-8.2}^{+7.8}$ days. The obtained magnification ratios are $\mu_{\text{S2/S1}} = 1.14 \pm 0.02$, $\mu_{\text{S3/S1}} = 1.01 \pm 0.02$, and $\mu_{\text{S4/S1}} = 0.35 \pm 0.02$. We estimate the Hubble constant $H_0 = 68.6_{-9.7}^{+13.6}$ km s^{−1} Mpc^{−1} via rescaling the time delays predicted by different lens models to match the values obtained in this work. With more photometric data on the fifth image SX, we will be able to further refine the time delay and magnification estimates for SX and obtain competitive constraints on H_0 .

Unified Astronomy Thesaurus concepts: Type II supernovae (1731); Strong gravitational lensing (1643); Galaxy clusters (584)

1. Introduction

Supernova (SN) explosions are among the most energetic and fascinating phenomena in the universe. Investigating these objects is essential not only for understanding the physics of stellar explosions but also for studying properties of progenitor population, stellar evolution, nucleosynthesis, modeling chemical evolution of galaxies, and origin of cosmic rays, to name a few. Throughout modern astrophysics, SNe have also been used to measure cosmological distances. Due to high intrinsic brightness and “standardizable” light curves (LCs), Type Ia SNe (SNe Ia) are now routinely used to determine cosmological parameters. It was by using SNe Ia that Riess et al. (1998) and Perlmutter et al. (1999) discovered an accelerated expansion of the universe. Observations of Type II SNe (SNe II) can be also used to determine distances to their host galaxies. Despite the fact that SNe II show large variations in their observational properties (luminosities, durations, etc.), there are a number of methods to utilize observations of SNe II for cosmological studies (see, e.g., Nugent & Hamuy 2017, for a review). For instance, the expanding photosphere method (EPM) was proposed by Kirshner & Kwan (1974) to measure distances to the Type II plateau SNe, whose LC is nearly flat for ~ 100 days and then suddenly drops off. The EPM has been successfully applied to nearby SNe IIP (e.g., Tsvetkov et al. 2019) and more distant objects (up to $z \simeq 0.34$; Gall et al. 2018). Other techniques include the spectral-fitting expanding atmosphere method (e.g., Baron et al. 2004) for SNe IIP and the dense shell method (Potashov et al. 2013; Baklanov et al. 2013) to measure distances to SNe IIn.

One of the current frontiers in SN research centers is constructing numerical models of SN explosions, reliability of which can be determined from comparison with observational data. Such SN modeling requires high-quality photometric and spectroscopic data. While for superluminous SNe (SLSNe) such detailed information can be in principle obtained even at high redshifts $z > 2$ (Cooke et al. 2012), this is not the case for SNe IIP, which are typically observed up to $z \sim 0.4$ (Nugent & Hamuy 2017). So far, hydrodynamical models of SNe IIP were constructed only for nearby objects.

Recent discovery of gravitationally lensed SNe with multiple images—SN Refsdal (Kelly et al. 2015) and SN iPTF16geu (Goobar et al. 2017)—opens up a window to the unexplored high-redshift transient universe. Strongly lensed SNe represent a class of objects unique for both astrophysics and cosmology. They not only make possible investigation of the properties of SN progenitors (pre-SNe) and their environments at high redshifts (a signal from which would not be detected in the absence of a lens) but also can be used for cosmological studies. In a case of a variable source such as an SN, LCs for different images are shifted in time relative to each other. By measuring these time delays between images, one can obtain an independent estimate of the Hubble constant (first suggested by Refsdal 1964) and the dark energy equation of state (e.g., Linder 2011). For certain types of SNe II and for SNe Ia, the intrinsic luminosities can be inferred independently of gravitational lensing. In such cases, the absolute lensing magnification can be constrained independently of a lens model, thus helping to break the degeneracy between the radial mass profile of a lens and the Hubble constant (Oguri & Kawano 2003). Indeed,

numerous studies of lensed quasars have convincingly shown that the Hubble constant value is sensitive to details of a lens model (e.g., Kochanek 2002; Larchenkova et al. 2011; Birrer et al. 2016; Wong et al. 2020, among others) and assuming a power-law density distribution (the simplest lens model) introduces a bias in the determination of H_0 (e.g., Xu et al. 2016).

This paper is devoted to radiation hydrodynamics modeling of the first discovered lensed SN with multiple images—SN Refsdal. Kelly et al. (2016) have already shown that the spectra and LC of SN Refsdal are similar to those of SN 1987A, a peculiar SN II in the Large Magellanic Cloud, and that the progenitor of SN Refsdal is most likely to be a blue supergiant (BSG). As emphasized in Rodney et al. (2016), none of the existing LC templates are able to capture all the features of the SN Refsdal LC, thus making the task of modeling of SN Refsdal important. Moreover, SN Refsdal was located in the arm of a spiral host galaxy at $z \simeq 1.5$, i.e., much farther away than any modeled Type II SNe so far. The construction of a physical model of the pre-SN, which satisfies available photometric observations in different filters, should in principle allow one to determine time delays between images more accurately than is done in Rodney et al. (2016) and to constrain the magnification factors. This information can serve as an independent test of different lens models presented in the literature (see Treu et al. 2016, for a compilation of lens models) and/or used as an additional constraint to improve the lens model. The latter should lead to an improved precision in determining the Hubble constant and other cosmological parameters (e.g., Grillo et al. 2018, 2020). The paper is organized as follows. In Section 2, we list available observational data on SN Refsdal. Section 3 gives a brief description of constructed hydrodynamical SN models, and the best-fit model that matches all available observational data is described in Section 3.1. Technical details on the fitting procedure are given in the Appendix. We use the reconstructed the SN Refsdal LC to derive time delay and magnification ratios for all images in Section 4. With these estimates in hand, we obtain the most likely Hubble constant value in Section 5. Finally, all the results of this work are summarized in Section 6.

2. Observations

A strongly lensed SN was found in the MACS J1149.6+2223 galaxy cluster field on 2014 November 10 (Kelly et al. 2015). The HST images revealed four resolved images of the background SNe ($z = 1.49$) arranged in an Einstein cross-configuration around a massive elliptical galaxy ($z = 0.54$)—an MACS J1149.6+2223 cluster member.

To construct a hydrodynamic model for SN Refsdal, we use photometric data from Rodney et al. (2016, their Table 4) obtained with HST using the Wide-Field Camera 3 (WFC3) with the infrared (IR) and UV–optical (UVIS) detectors and the Advanced Camera for Surveys (ACS).

The dynamical properties of the envelope and characteristic expansion velocities can be obtained by investigating line profiles in the spectra of the SN. Thanks to gravitational amplification of the SN Refsdal light, there are HST, Keck, and VLT X-shooter spectra (Kelly et al. 2016) available. Despite being noisy, these spectral observations give us constraints on how the velocity of the envelope was changing during the epoch of maximum light in the F160W band. We use the $H\alpha$

expansion velocity measurements from Kelly et al. (2016) in Section 3 to constrain the model parameter space.

In the direction of SN Refsdal dust absorption in our Galaxy is insignificant, with $E(B - V)_{\text{MW}} = 0.02$ (Lotz et al. 2017). This is not surprising, since for observations of distant objects, such as the galaxy cluster MACS J1149.5+2223, it is natural to choose transparency windows in the Galaxy. Unfortunately, there is no information on dust extinction for SN Refsdal, and theoretical LCs presented in this work were not corrected for the host reddening. One way to account for $E(B - V)_{\text{host}}$ would be to include it as a fit parameter. For example, Rodney et al. (2016) added magnitude shifts as free parameters for each photometric passband to account for any color difference between a template and SN Refsdal. However, such an approach seems not to be optimal for our task—to model SN Refsdal LCs in various photometric bands self-consistently.

3. Supernova Simulation

SN Refsdal LCs demonstrate the slow rise in brightness to a broad peak. Combining this information with the analysis of $H\alpha$ emission and absorption features, Kelly et al. (2016) and Rodney et al. (2016) have already shown that SN Refsdal is a peculiar SN 1987A-like SN. SN 1987A, in its turn, is classified as a peculiar Type II Plateau SN with a progenitor being a BSG, rather than a red supergiant as for ordinary Type II-P SNe. SN 1987A has been intensively studied in recent decades (e.g., Utrobin 2005; for a review see McCray & Fransson 2016).

For the model calculation, we use the multigroup radiation hydrodynamics numerical code STELLA (Static Eddington-factor Low-velocity Limit Approximation; Blinnikov & Sorokina 2004; Baklanov et al. 2005; Blinnikov et al. 2006). STELLA allows one to construct synthetic LCs in various photometric bands and takes into account available observational constraints on the expansion velocity (coming from the analyses of P Cygni profiles), i.e., with STELLA we can utilize all the available SN Refsdal observational data. STELLA has been successfully used for a wide variety of SN studies including but not limited to SLSNe, pulsational pair-instability SNe (PPSNe), SNe Ia, and SNe IIP (Woosley et al. 2007a, 2007b; Sahu et al. 2008; Tominaga et al. 2011; Baklanov et al. 2015; Sorokina et al. 2016).

Note that STELLA is 1D and does not allow us to take into account any changes in a chemical composition that are caused by explosion-driven Rayleigh–Taylor instabilities and a shock wave passage through the SN shell. Moreover, for SN 1987A-like SNe the formation of a magnetar at the center of the SN shell is possible (Chen et al. 2020). That leads to an additional mixing of metals and complicates the distribution of chemical elements in the shell. Thus, we use “non-evolutionary” SN models and artificially reproduce details of the evolutionary models, as well as mixing during an explosion.

As the initial model of chemical composition and density profile, we use the well-studied pre-SN model of Nomoto & Hashimoto (1988) and Saio et al. (1988) and the explosive nucleosynthesis model of Shigeyama & Nomoto (1990). Blinnikov et al. (2000) performed a detailed analysis of SN 1987A and showed that an explosion of the evolutionary model of Nomoto & Hashimoto (1988) allows one to reproduce with enough precision SN 1987A LCs and dynamical properties of the expanding shell. Mixing of ^{56}Ni and hydrogen is an important ingredient of a pre-SN model since it has a significant impact on the shape of an LC and on the observed gamma and X-ray radiation of SN 1987A (Bartunov et al. 1987; Kumagai et al. 1989; Shigeyama & Nomoto 1990). To

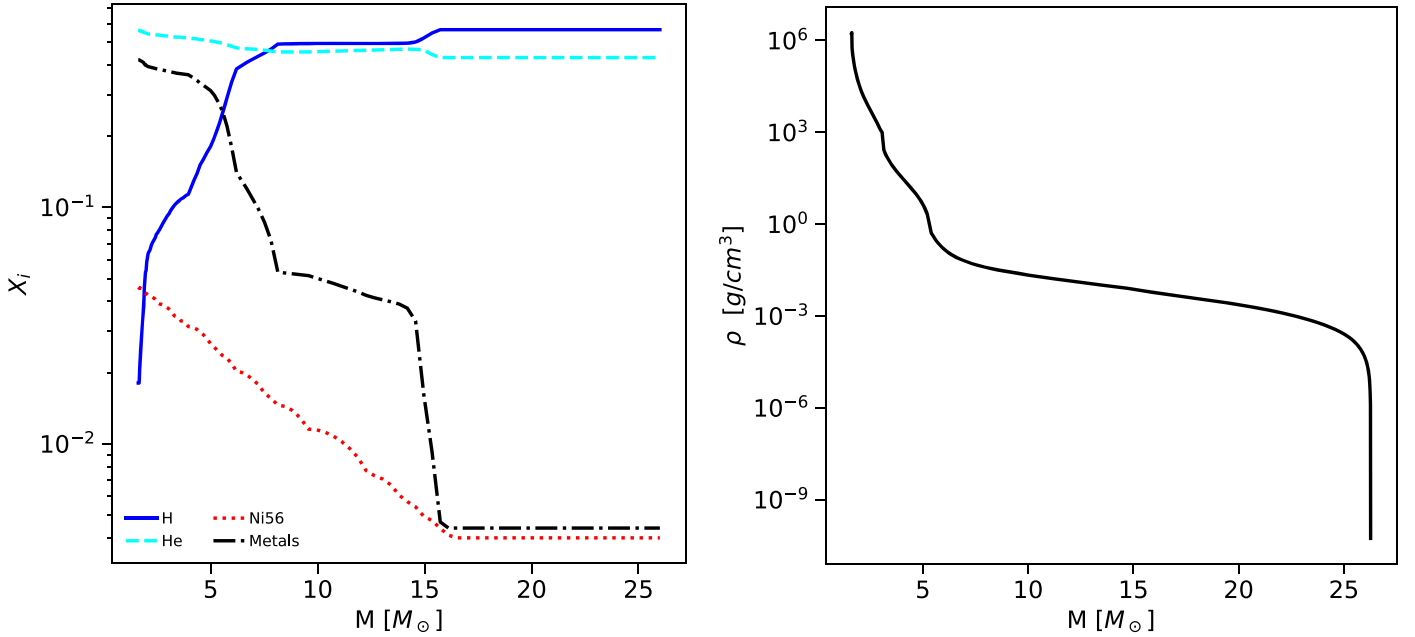


Figure 1. Left panel: mass fraction of hydrogen (blue solid line), helium (cyan dashed line), heavy elements (black dashed–dotted line), and radioactive ^{56}Ni (red dotted line) in the ejecta of model M1 (the model that best reproduces the observed SN Refsdal LCs; see Section 3.1). Right panel: density distribution of model M1 as a function of interior mass. The total mass of the pre-SN is $M_{\text{tot}} = 26.3 M_\odot$, $M_{^{56}\text{Ni}} = 0.25 M_\odot$, and the mixing is artificial. After an explosion, a proto–neutron star core with a mass of $1.6 M_\odot$ is left.

obtain an LC with a broad dome-shaped maximum, one needs to mix ^{56}Ni closer to the edge of the envelope and hydrogen down to the central region. Then, the radioactive decay of ^{56}Ni would start heating and ionizing material at the shell edge just after the shock breakout, and the hydrogen-recombination front would exist for a longer period. This would cause an increase in the photosphere radius. Note that a similar approach to mixing of ^{56}Ni was used in Utrobin & Chugai (2011) to explain the LC and spectroscopic data of SN 2000cb, which is also a peculiar SN 1987A-like SN and characterized by a wide dome-like LC maximum. Following Baklanov et al. (2005), we constructed the BSG models in non-evolutionary hydrostatic equilibrium by varying masses of hydrogen and helium in the outer shell. Typical chemical composition and density distribution in our SN models are shown in Figure 1.

The explosion was triggered using the “thermal bomb” model (Shigeeyama & Nomoto 1990; Blinnikov et al. 2000), namely, via a short ($\Delta t_{\text{burst}} = 0.1\text{s}$) release of thermal energy E_{burst} in the near-central layers with the mass of $0.06 M_\odot$ on the outer edge of the core with a mass of $M_{\text{core}} = 1.6 M_\odot$ (Blinnikov et al. 2000). The core material forms a proto–neutron star and does not participate in the expansion of the SN envelope. In the equations of motion of the envelope material, the contribution of the core to the gravitational potential is taken into account.

To obtain the model that simultaneously reproduces multi-band SN Refsdal LCs, we computed a set of 185 radiation hydrodynamical models. SN Refsdal is a gravitationally lensed SN, and the absolute magnifications of its images are poorly constrained. For example, the absolute magnification for S1 predicted by different lens models⁶ (Oguri 2015; Kawamata et al. 2016; Sharon & Johnson 2015; Jauzac et al. 2016;

⁶ Note that the range of magnifications provided here does not appear to be exhaustive, since absolute magnifications are not available in the literature for all the lens models.

Table 1
Parameter Space of Our 185 SN Models

	R_0 (R_\odot)	M_{tot} (M_\odot)	$M_{^{56}\text{Ni}}$ (M_\odot)	E_{burst} (E51)	Z
Min	30	16	0.077	1	0.001
	\vdots	\vdots	\vdots	\vdots	\vdots
Max	100	27	0.42	7	0.005

Note. The parameter space of our 185 SN models: minimum and maximum values of the radius and total mass of the pre-SN, ^{56}Ni mass, total explosion energy (in units of 10^{51} erg), and metallicity, defined as the mass fraction of elements heavier than helium in the outer shells of a pre-SN.

Grillo et al. 2016) is $\mu_{S1} \sim 10 \div 25$. Thus, we cannot use the observed peak luminosity as a constraint. Instead, we try to reproduce the shape of SN Refsdal LCs in different bands, keeping in mind estimates available in the literature of the absolute magnifications for S1 and measured in the Kelly et al. (2016) $H\alpha$ expansion velocity. The ranges of values of the SN model parameters are given in Table 1. Note that the parameters are not distributed uniformly in the parameter space, but converge to some optimal model (in the sense of Bayesian evidence; see the Appendix). At each time step, STELLA calculates the spectral energy distributions (SEDs), which are then transformed from host galaxy rest frame ($z = 1.49$) into the observer’s frame and convolved with the transmission functions of the HST filters. Here, we use the F105W, F125W, and F160W bands since the coverage of the Refsdal LC in these bands is most complete and well sampled.

3.1. Best-fit SN Refsdal Model

Our procedure to find the best-fit model (as well as the time delays and magnification ratios) is described in detail in the Appendix. Here, we just outline the main steps. For each computed SN model, we compare synthetic LCs with observations and

Table 2
Mean Values of SN Model Parameters Computed Using the Bayesian Model Averaging Method and the Parameters of the Best-fit Model M1

	$R_0 (R_\odot)$	$M_{\text{tot}} (M_\odot)$	$M_{\text{ej}} (M_\odot)$	$M_{^{56}\text{Ni}} (M_\odot)$	$E_{\text{burst}} (E_{51})$	Z
BMA	50 ± 1	25 ± 2	23.4 ± 2	0.26 ± 0.05	4.7 ± 0.8	0.005 ± 0.015
Best fit	50	26.3	24.7	0.247	5	0.004

maximize the likelihood function (A1) with five free parameters: the absolute time and magnitude shifts for the reference image S1, and the model photometric uncertainties in three HST passbands used (see the Appendix for a discussion of why model uncertainties are introduced as fit parameters). As the priors for all the fit parameters, we use uniform distributions spanning a wide range of values. Then, we determine the time and magnitude shifts of images S2–S4 relative to S1 in a similar fashion. Next, we calculate the posterior probability of each SN model and use the obtained value as a measure of how well the model fits observations. We report the eight best-performing SN models with corresponding posterior probabilities in Table 4 and show the model LCs in comparison with observations in the Appendix (see Figure 8). To obtain the mean pre-SN parameters and estimate their uncertainties, we use the Bayesian model averaging (BMA) approach (Hoeting et al. 1999), which basically provides a weighted average for each parameter of interest, incorporating the posterior probabilities in the weighting (see the Appendix for details). The BMA results are provided in Table 2. Since model M1 significantly outperforms all other explored models (see Column (2) of Table 4), the BMA values are quite close to the best-fit parameters. Below we discuss in detail particular models constructed in this work.

Model M1 fits best to the observed SN Refsdal LCs, and the resulting photospheric velocity is in agreement with available H α expansion velocity measurements from Kelly et al. (2016). The photospheric velocity can be inferred from a blueshift of weak absorption lines such as the lines of Fe II $\lambda\lambda$ 5018 and 5169. For SNe IIP, including peculiar SN 1987A-like SNe, the Fe II lines show systematically lower velocities compared to H α (Blanco et al. 1987; Taddia et al. 2012). Therefore, H α velocities should be systematically higher than the photospheric velocities of our models.

The main parameters of the best-fit model M1 are the following: the total mass $M_{\text{ej}} = 26.3 M_\odot$, the ejecta mass $M_{\text{ej}} = 24.7 M_\odot$, the pre-SN radius $R_0 = 50 R_\odot$, the ^{56}Ni mass $M_{^{56}\text{Ni}} = 0.25 M_\odot$, and the explosion energy $E_{\text{burst}} = 5 \times 10^{51}$ ergs (listed in Table 2).

BSGs are compact, and the time of shock breakout is ≈ 1.25 hr with a boundary velocity of $\approx 59,000$ km s $^{-1}$ (see Figure 2). Soon after the shock breakout at $t \approx 1.4$ hr, the radiative losses became small compared to the kinetic energy of the shell. Thus, internal temperature in the shell falls almost adiabatically, while the bolometric luminosity decreases to 7×10^{41} erg s $^{-1}$ and then reaches its local minimum at day 1 after the explosion (see Figure 2, left panel). Details of the explosion model (the duration of the energy release and the mass of the thermal bomb) significantly influence the magnitude and the shape of the first maximum of the LC. For the SN Refsdal modeling, these parameters are relatively inessential, since observations started during the rise toward the second maximum of the LC (cupola), which forms determined by properties of the cooling and recombination wave and the contribution of radioactive ^{56}Ni decay.

Our $M_{^{56}\text{Ni}} = 0.25 M_\odot$ estimate is within the range of $(0.005 - 0.28)M_\odot$ implied by the observed distribution of $M_{^{56}\text{Ni}}$ for SNe II (Müller et al. 2017) and is consistent with the high energy of explosion (Sukhbold et al. 2016). Note that the total energy release in M1 is greater than 2×10^{51} erg, i.e., beyond the range implied by neutrino-driven explosions (Sukhbold et al. 2016). Sukhbold et al. (2016) found that at most 6%–8% of the SN IIP explosions are connected to progenitors more massive than $20 M_\odot$ when they used SN 1987A-calibrated neutrino engines. However, a typical evolutionary scenario for a single star with a total mass of $\sim 26 M_\odot$ does not lead to a BSG stage before an SN explosion. The low-metallicity models (Hillebrandt et al. 1987) or a merger of a compact binary system (Menon et al. 2019) could explain the appearance of the BSG pre-SN. Nevertheless, M1 with $M_{\text{ej}} = 24.7 M_\odot$ is quite similar to other well-explored peculiar SN 1987A-like SNe, with many of them having $M_{\text{ej}} > 20 M_\odot$ (Taddia et al. 2012).

Metallicity⁷ in the outer layers of the M1 envelope is reduced by a factor of 5 ($Z_{M1} = 0.004$) relative to the solar metallicity ($Z_\odot = 0.02$) and is comparable to the value ($Z = 0.005$) of the model by Saio et al. (1988). The decline in the metallicity in the outer layers leads to the reduction of the line opacity, which is calculated in STELLA as expansion opacity following Eastman & Pinto (1993). While the cooling and recombination waves are propagating, the contribution of line opacity to the total opacity is significant. The line opacity drops dramatically from UV toward optical wavelengths. Thus, lower metallicity mainly affects the LCs in blue and UV LCs, which allowed us to reproduce the LCs in the F814W band (see Figure 2, right panel).

According to our best-fit model, the absolute magnification of the S1 image is $\simeq 10$ (see Column (8) of Table 5), which is within the range of magnifications $\mu_{S1} \sim 10 \div 25$ predicted by different lens models (Oguri 2015; Kawamata et al. 2016; Sharon & Johnson 2015; Jauzac et al. 2016; Grillo et al. 2016). To increase the absolute magnification of S1, we should reduce a radiated flux. Model M4 (see Table 4) has $M_{^{56}\text{Ni}} = 0.12 M_\odot$ in the envelope, i.e., ~ 2 times less than the best-fit model. Thus, the amount of heat released as a result of ^{56}Ni decay is also ~ 2 times lower, and a smaller amount of energy can be radiated. M4 fits the SN Refsdal LCs if the absolute magnification of S1 is $\mu_{M4} = 18.6$, i.e., ~ 2 times larger than for M1 (see Figure 8 in the Appendix). In principle, the amount of ^{56}Ni and, as a consequence, the absolute magnification can be constrained from spectral lines (Utrobin & Chugai 2011) or by the slope of the tail of the SN LCs (Nadyozhin 2003).

4. Time Delays and Magnification Ratios

4.1. SN Refsdal Images S1–S4

In the previous section, for each computed SN model we derived the best-fit absolute time and magnitude shifts for image

⁷ Throughout this work, metallicity Z is defined as the mass fraction of elements heavier than helium in the outer shells of a progenitor.

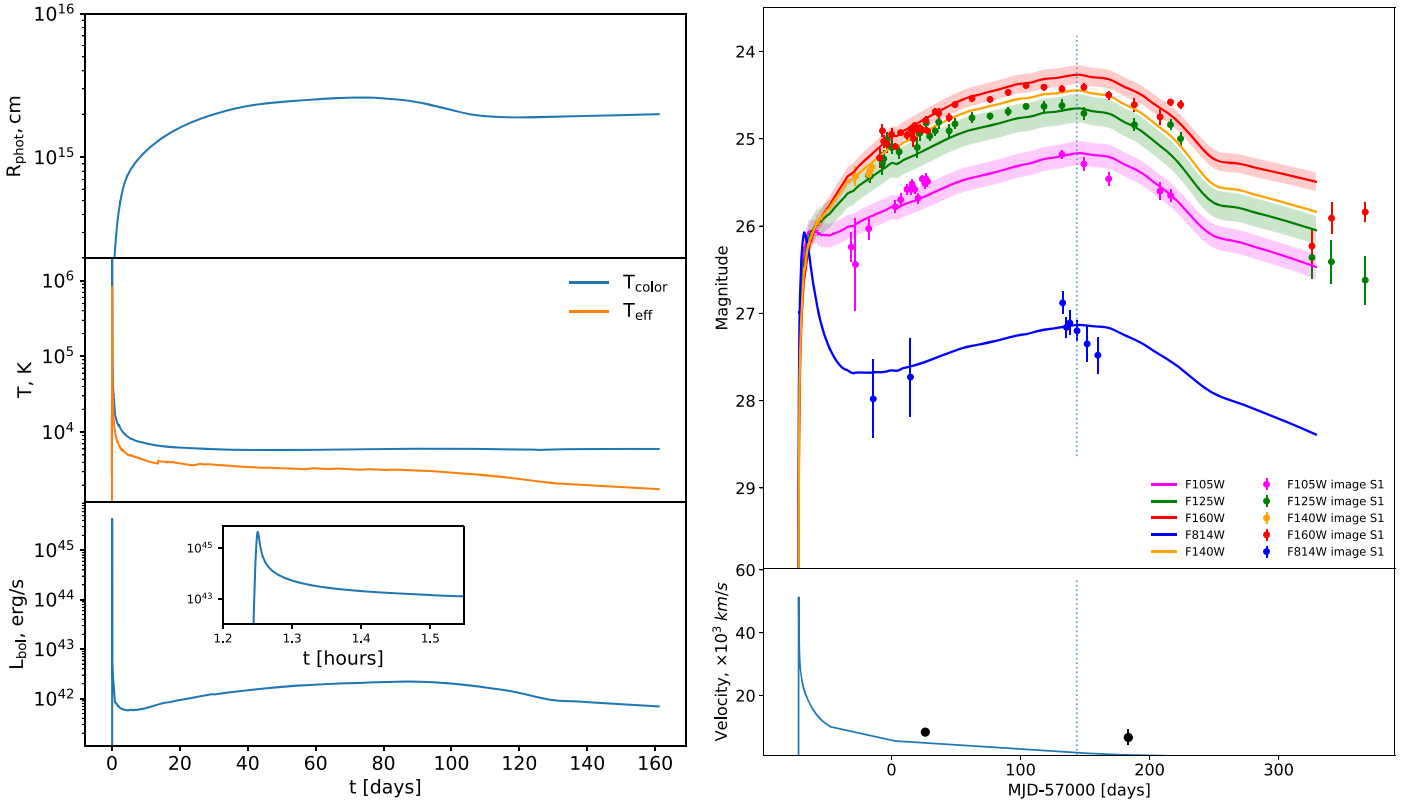


Figure 2. Observational properties of the best-fit model M1. The left panel shows the photospheric radius, the color and effective temperature, and the bolometric luminosity. The top panel on the right shows the multiband photometry for the S1 image, and the bottom panel demonstrates the evolution of the photosphere velocity in comparison with $H\alpha$ expansion velocity measurements (black circle) from Kelly et al. (2016). The vertical dotted line marks the date of the peak brightness in F160W. Note that observed LCs in all filters are well reproduced by M1, although for fitting we used only F160W, F125W, and F105W passbands (these filters are shown with the model uncertainties).

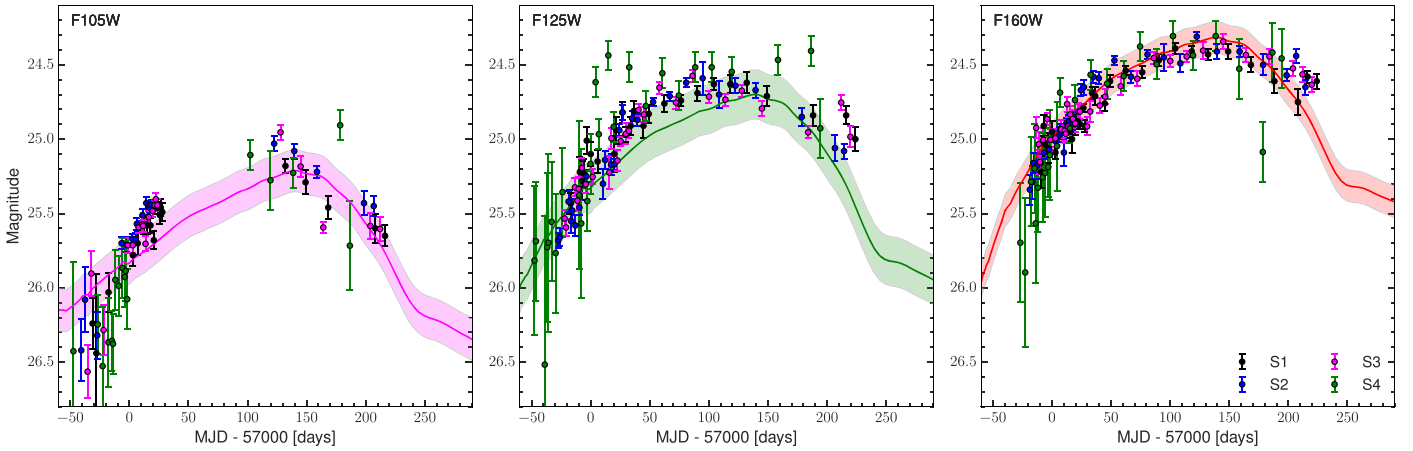


Figure 3. Composite LCs from images S1–S4 after applying the magnitude and time shifts (relative to the image S1) determined for the best-fit model M1. Measurements for S1–S4 are shown, respectively, in black, blue, magenta, and green. The best-fit model LCs are shown as solid lines, with photometric uncertainties as shaded areas.

S1. By fitting the model LCs to images S2, S3, and S4, we obtained the time shifts and magnifications of images S2–S4 relative to S1 (for details, see the Appendix). Figure 3 illustrates the results of our time delay and magnification calculations for the best-fit model M1. Each panel shows the composite LC from images S1–S4, after applying the time and magnitude shifts so that S2–S4 match the S1 LC. The best-fit model LCs are overplotted as red (F160W filter), green (F125W), and magenta (F105W) lines, with the shaded bands indicating the model uncertainty. The photometric model uncertainties in each filter

for the best-fit model are provided in the Appendix, Table 4 (see the first row).

To derive a single measurement of the time delay and magnification ratio for SN images that takes into account the Bayes factor and the uncertainty of each SN model, we use the BMA method (Equations (A4)–(A5)). Mean values of time delays and magnification ratios obtained from the BMA combinations are provided in Table 3.

Thanks to the discovery of the first multiply-lensed SN, the galaxy cluster MACS 1149.5+2223 has been extensively

Table 3
Summary of Time Delay and Magnification Ratio Measurements

Parameter	BMA Mean	Template Fits ^a	Polynomial Fits ^a
MJD _{pk} (days)	57144 ⁺¹⁰ ₋₁₀	57138 ± 10	57132 ± 4
Δt _{S2-S1} (days)	9.5 ^{+2.6} _{-2.7}	4 ± 4	7 ± 2
Δt _{S3-S1} (days)	4.2 ^{+2.3} _{-2.3}	2 ± 5	0.6 ± 3
Δt _{S4-S1} (days)	30 ^{+7.8} _{-8.2}	24 ± 7	27 ± 8
Δt _{SX-S1} (days)	340 ⁺⁴³ ₋₅₂
μ _{S2/S1}	1.14 ^{+0.021} _{-0.020}	1.15 ± 0.05	1.17 ± 0.02
μ _{S3/S1}	1.01 ^{+0.019} _{-0.018}	1.01 ± 0.04	1.00 ± 0.01
μ _{S4/S1}	0.35 ^{+0.016} _{-0.015}	0.34 ± 0.02	0.38 ± 0.02
μ _{SX/S1}	0.24 ^{+0.12} _{-0.07}

Note. Summary of time delay and magnification ratio measurements. The second column presents results obtained in this work in comparison with estimates obtained in Rodney et al. (2016) via LC template fitting and polynomial fits.

^a Values from Rodney et al. (2016, see their Table 3).

observed and modeled by several independent lens teams (see, e.g., Oguri 2015; Kawamata et al. 2016; Sharon & Johnson 2015; Grillo et al. 2016; Jauzac et al. 2016). Comparison of lens models and summary of the time delays and magnification ratios predicted by those models are given in Treu et al. (2016). Figure 4 presents a comparison of our measured mean time delays and magnification ratios for SN Refsdal images S1–S4 against the lens model predictions from Treu et al. (2016) (namely, “Die-a,” “Gri-g,” “Ogu-a,” “Ogu-g,” “Sha-a,” “Sha-g”). The estimates of the time delay and magnification ratios resulting from the template and polynomial fitting (Rodney et al. 2016) are also shown. Our time delays and magnification ratios of the SN Refsdal multiple images S1–S4 are consistent, within the errors, with results of Rodney et al. (2016) (see Table 3).

4.2. SX

Approximately a year after the discovery of SN Refsdal “Einstein cross,” a fifth image appeared. As it was expected, SX is much fainter than S1–S4, and its photometric measurements are scarce. To place constraints on the time delay and magnification of SX relative to S1, we use, on the one hand, available SX photometry from Kelly et al. (2016, see their Table 1) in F125W and F160W filters and, on the other, information about SX brightening, registered in 2016 January (Kelly et al. 2016). We repeat the procedure of maximizing the likelihood function (see the Appendix) to find the best-fit values of the time and magnitude shifts of SX relative to S1 for eight best-fit SN models. The eight best-performing models are illustrated in Figure 9, and Figure 10 shows the marginal distributions for the SX–S1 time delay and the SX magnification for the best-fit model M1. The obtained marginalized distributions are quite broad (for all best-performing models, not only for M1), and as a consequence, uncertainties on the parameters of interest are large. Due to a broad peak, the model LCs in F125W and F160W filters are relatively featureless, and two to three data points are not enough to obtain tight constraints.

We again calculate the mean values using the BMA method. The time delay and the magnification of SX are $\Delta t_{SX-S1} = 340^{+43}_{-52}$ days, $\mu_{SX/S1} = 0.24^{+0.12}_{-0.07}$. In Figure 5, we plot the best-fit model M1 and BMA estimates of the time delay and magnification

ratio between images S1 and SX in comparison with the constraints from Kelly et al. (2016) and lens model predictions from several teams reported by Treu et al. (2016).

5. Hubble Constant

More than half a century ago Refsdal (1964) proposed to use time delays between multiple images of gravitationally lensed SNe to measure the Hubble constant. However, no multiply-imaged SN has ever been observed until just recently. In practice, the strong lens time delay cosmography has been employed extremely successfully for decades using multiply-imaged quasars. For example, the H0LiCOW collaboration (Suyu et al. 2017) has recently constrained H_0 to 2.4% precision for a flat Λ CDM cosmology from a joint analysis of six gravitationally lensed quasars with measured time delays (Wong et al. 2020). To achieve such a precision, one needs a variety of observational data. For example, to measure time delays between images, several years of photometric monitoring of the lens system are typically required, because the LCs of quasars are stochastic and heterogeneous and their intrinsic stochasticity is hard to disentangle from variability due to microlensing (e.g., Eigenbrod et al. 2005; Tewes et al. 2013; Dobler et al. 2015, among others). In contrast to quasars, gravitationally lensed SNe with multiple images occur on short timescales, allowing their time delays to be measured with far fewer observational efforts. Moreover, after lensed SNe fade away, one can obtain imaging of a host galaxy to validate the lens model. In addition, the intrinsic luminosities of SNe Ia and of certain types of core-collapse SNe can be determined independently of lensing, which allows us to directly measure the lensing magnification factor. A model-independent estimate of the magnification can improve constraints on the lens model especially for galaxy clusters with only a few known multiple-image systems (Riehm et al. 2011).

Here, we constrain the Hubble constant using the values of time delays between SN Refsdal images determined in Section 4. While modeling the SN Refsdal LCs and determining time delays between images, we have ignored the microlensing effect. A preliminary assessment of whether there are any indications of especially strong microlensing events that could bias time delay and magnification measurements is given in Rodney et al. (2016). They concluded that the SN Refsdal LCs are unlikely to be affected by major microlensing events. Throughout the paper, we assume that microlensing has no influence on our results, but there are studies that show that microlensing does indeed introduce uncertainty in the time delay and the Hubble constant measurements (see, e.g., Dobler & Keeton 2006; Goldstein et al. 2018; Pierel & Rodney 2019). Huber et al. (2019) and Suyu et al. (2020) discuss the best strategies to detect gravitationally lensed SNe and to measure their time delays with high accuracy in the presence of microlensing.

To derive H_0 , we follow the approach proposed in Vega-Ferrero et al. (2018), where the Hubble constant is obtained via rescaling the time delay predictions of the lens models to match the observed values (although see Grillo et al. 2018 for discussion on possible caveats of this approach). The following lens models are considered here: “Gri-g,” “Ogu-g,” “Ogu-a,” “Sha-g,” and “Sha-a.” Descriptions of these models, time delays, and magnification predictions for all SN Refsdal images are given in Treu et al. (2016, see their Table 6). Following Vega-Ferrero et al. (2018), we estimate the probability of H_0 given “observational” data D (i.e., the obtained best-fit values

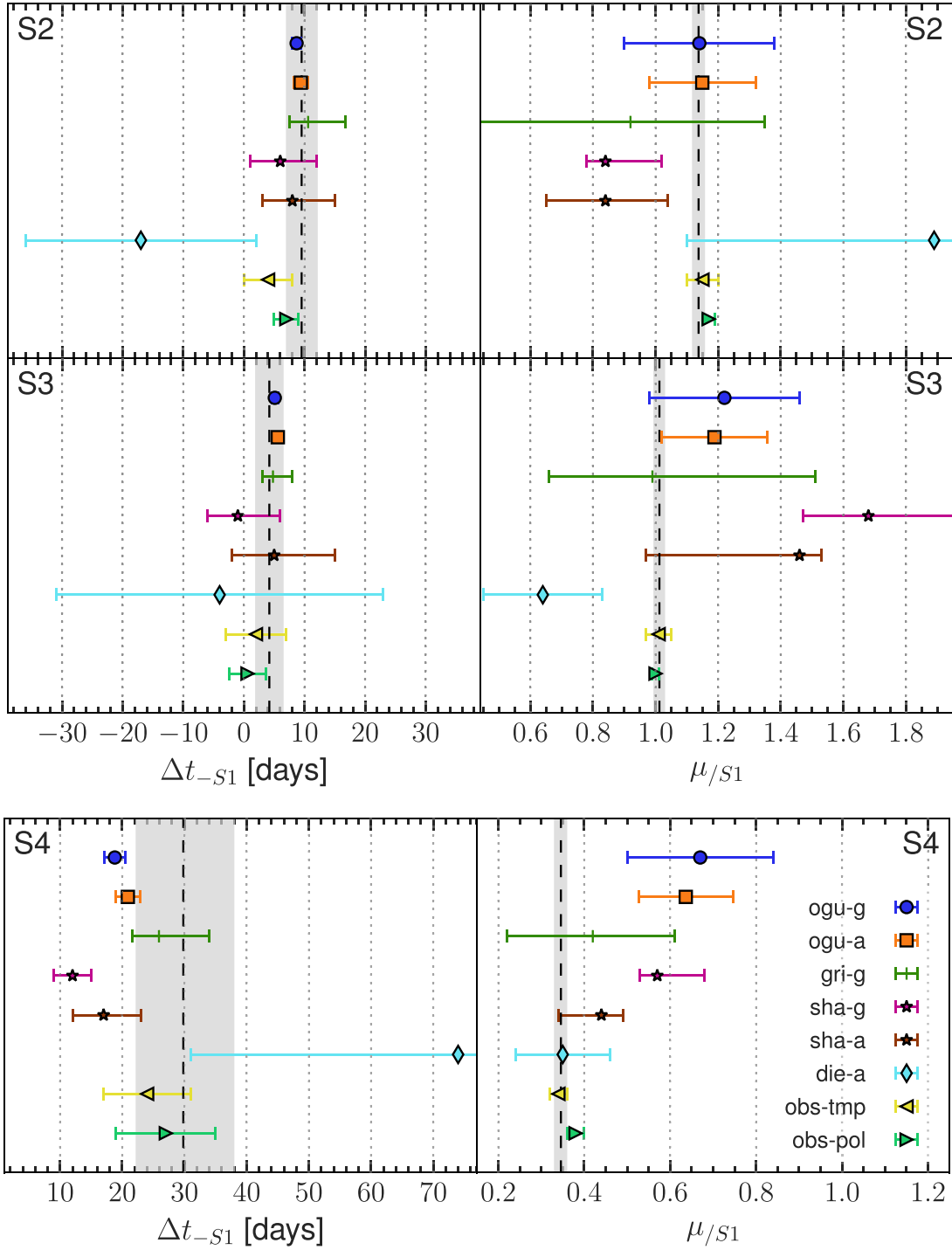


Figure 4. Comparison of lens model predictions from the literature with time delay and magnification values obtained in this work. The left and right columns present the time delays and magnification ratios (both relative to S1), correspondingly. Results for images S2, S3, and S4 are shown from top to bottom. The dashed vertical lines and the gray shaded regions indicate our best estimate of the time delay/magnification ratio with uncertainties (see Column (2) of Table 3). Values predicted by different lens models (“Die-a,” “Gri-g,” “Ogu-a,” “Ogu-g,” “Sha-a,” “Sha-g”) are plotted as colored symbols (see the legend in the bottom right panel). Yellow and green triangles mark the measurements from Rodney et al. (2016) derived from LC template (“obs-tmp”) and polynomial (“obs-pol”) fitting, correspondingly.

of Δt and μ listed in Table 3) as

$$\begin{aligned}
 P(H_0|D) &\propto P(H_0) P(D|H_0) \\
 &\propto P(H_0) \int d\Delta t d\mu \cdot p_{\text{lens}}(\Delta t, \mu|H_0) \cdot p_{\text{obs}}(\Delta t, \mu), \quad (1)
 \end{aligned}$$

where $P(H_0)$ is the prior for H_0 (assumed to be flat between 20 and 120 km s⁻¹ Mpc⁻¹), $p_{\text{lens}}(\Delta t, \mu)$ is the distribution of time

delay and magnification predictions of a given lens model (which can be rescaled to any alternative value of H_0), and $p_{\text{obs}}(\Delta t, \mu)$ is the “observational” distribution obtained in this work. We assume that for each lens model $p_{\text{lens}}(\Delta t, \mu)$ is described with a normal bivariate distribution (with no correlation between Δt and μ). The mean values and their statistical uncertainties for each image are taken from Table 6

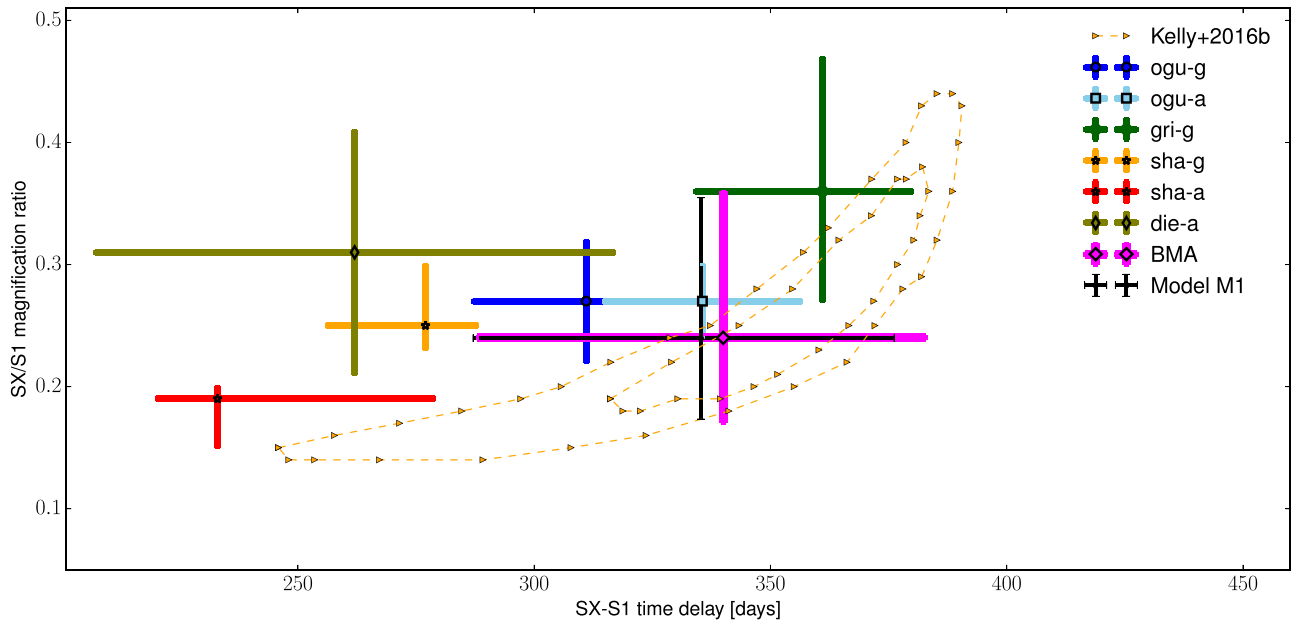


Figure 5. Best-fit model M1 and BMA constraints (in magenta) on the time delay and magnification of the image SX relative to S1. 1σ and 2σ orange contours show results from Kelly et al. (2016), where the shape of the LC was obtained via fitting second-order polynomials to S1 measurements in F125W and F160W bands separately. Values predicted by different lens models are plotted as colored points (see the legend in the upper right corner).

of Treu et al. (2016). To obtain the “observed” distributions $p_{\text{obs}}(\Delta t)$ and $p_{\text{obs}}(\mu)$, we average marginalized distributions of all explored SN models using the BMA method with weights corresponding to posterior probabilities of SN models (see the Appendix). Figure 6 shows the obtained $P(D|H_0)$ for different lens models for each image separately (top and middle panels) and the “combined” $P(D|H_0)$ distributions (bottom left panel) calculated as a product of $P(D|H_0)$ for separate images. The total posterior distribution $P_+(H_0|D)$ (see the bottom right panel of Figure 6) is calculated as the mean of “combined” $P(D|H_0)$ distributions for lens models. The median value and 68% for the Hubble constant are $68.6^{+13.6}_{-9.7} \text{ km s}^{-1} \text{ Mpc}^{-1}$. We see that the lens models “Ogu-g,” “Ogu-a,” and “Gri-g” contribute most to the total $P_+(H_0|D)$, i.e., these models are in a good agreement with time delays and magnification ratios obtained in this work.

With more photometric measurements of the image SX, we will be able to drastically improve our time delay and magnification measurements, as well as accuracy of H_0 determination.

6. Conclusions

Hydrodynamic simulation of the LCs and the expansion velocities allows us to get significant insights into the nature of core-collapse SN progenitors, namely, to estimate the radius and the mass of a progenitor star, an explosion energy, an ejecta mass, and a radioactive ^{56}Ni amount. At high redshifts, core-collapse SNe, especially Type IIP, are hard to discover owing to their faintness. The highest-redshift spectroscopically confirmed SN IIP is PS1-13bni with a redshift of $z = 0.335^{+0.009}_{-0.012}$ (Gall et al. 2018). With the help of gravitational lensing, we can probe SNe IIP at much greater distances. Before the discovery of SN Refsdal, the highest-redshift core-collapse SN (most likely Type IIP) was at $z \simeq 0.6$ (Stanishev et al. 2009). This transient was found in the A1689 galaxy cluster field and probably was magnified by ~ 1.4 mag. Unfortunately, its LC is poorly sampled to perform a detailed analysis. The discovery of SN Refsdal offered us a unique

opportunity to model such a distant SN ($z = 1.5$) and to study properties of its progenitor. We modeled SN Refsdal using the multigroup radiation hydrodynamics numerical code STELLA, which allows one to construct synthetic LCs in various photometric bands and accounts for the expansion velocity of the $\text{H}\alpha$ shell. For the first time, we obtained the hydrodynamic model of an SN IIP at a cosmologically relevant distance. We computed a set of 185 hydrodynamical models covering a rather large area in the parameter space. We confirm the conclusion of Kelly et al. (2016) that SN Refsdal is a more energetic version of SN 1987A. Our calculations suggest that the SN Refsdal progenitor was a BSG with a radius of $R_0 = (50 \pm 1)R_\odot$, total mass of $M_{\text{tot}} = (25 \pm 2)M_\odot$, radioactive ^{56}Ni mass of $M^{56\text{Ni}} = (0.26 \pm 0.05)M_\odot$, and total energy release of $E_{\text{burst}} = (4.7 \pm 0.8) \times 10^{51} \text{ erg}$ (parameters were obtained via the BMA method).

Future deep surveys should be able to detect a large number of gravitationally lensed SNe, including Type IIP, at high redshifts. Analysis of their LCs should allow us to compare high- z SNe with the local IIP population to investigate any systematic difference between high- and low-redshift SNe.

Proper reconstruction of SN Refsdal LC allowed us obtain relative time delays and magnification ratios between images S2–S4 and S1. Mean values (obtained via the BMA method) with uncertainties are provided in Table 3. We anticipated that we would be able to constrain the time delay of the fifth SN Refsdal image SX and its magnification relative to S1 with an accuracy of several percent. Unfortunately, quite a broad “featureless” peak of the LC combined with very scarce photometric measurements for SX resulted in large uncertainties for parameters of interest. We obtain (again, using the BMA method) $\Delta t_{\text{SX-S1}} = 340^{+43}_{-52} \text{ days}$ and $\mu_{\text{SX/S1}} = 0.24^{+0.12}_{-0.07}$. Following the approach suggested in Vega-Ferrero et al. (2018), we computed the Hubble constant $H_0 = 68.6^{+13.6}_{-9.7} \text{ km s}^{-1} \text{ Mpc}^{-1}$ via rescaling the time delay predictions of the lens models to match the values obtained in this work. With

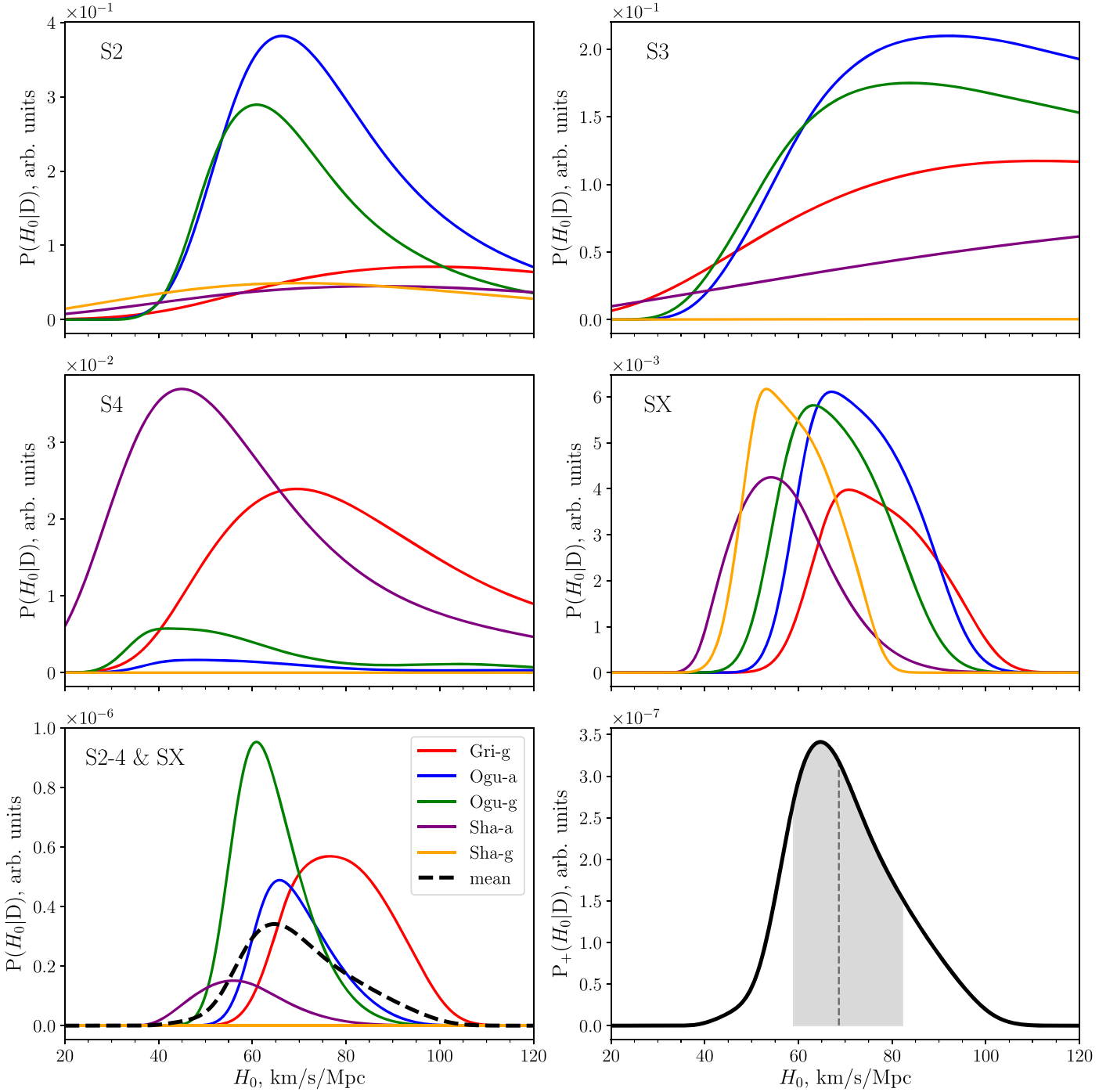


Figure 6. $P(D|H_0) = \int p_{\text{lens}}(\Delta t|H_0) \cdot p_{\text{obs}}(\Delta t) d\Delta t \times \int p_{\text{lens}}(\mu) \cdot p_{\text{obs}}(\mu) d\mu$ for different lens models calculated for images S2, S3, S4, and SX separately. Lens models are shown with different colors as indicated in the legend in the bottom left panel. Bottom left panel: combined contributions (from all images) of lens model predictions to the posterior distribution $P_+(H_0|D)$, shown in the bottom right panel. Bottom right panel: total posterior distribution $P_+(H_0|D)$ defined as the mean of likelihood functions $P(D|H_0)$ of different lens models. The dashed line marks the median value of H_0 . The gray shaded area denotes the 16th and 84th percentile confidence band. The best value for H_0 resulting from the combined analysis of all images is $68.6^{+13.6}_{-9.7} \text{ km s}^{-1} \text{ Mpc}^{-1}$.

more photometric data on SX, the accuracy of H_0 determination can be drastically improved.

Next-generation telescopes may provide not only detailed photometric LCs of lensed SNe IIP with resolved images but also high-quality spectra, which are necessary to determine photospheric velocities at several epochs. With such information, one can significantly improve a pre-SN model and, as a consequence, obtain a reliable estimate of an absolute magnification of SN images. The latter, in its turn, serves as

a powerful constraint for lens models. Altogether, reliable pre-SN and lens models ensure robust and accurate determination of the Hubble constant. At the same time, SNe IIP themselves with measured photospheric velocities can be used as direct distance indicators (e.g., Nugent & Hamuy 2017). The same techniques can be applied to lensed SNe IIP if the lens magnification is known. Thus, even a single-lensed SN IIP with spectral information available may in principle provide two independent probes of H_0 .

The authors are grateful to Masamune Oguri and Tatiana Larchenkova for many helpful discussions and Surhud More for valuable comments, which helped to improve the paper. P.B. is grateful to Ken’ichi Nomoto for the possibility of working at the Kavli IPMU, and his research on the supernova simulations has been supported by grant RSF 18-12-00522. S.B. is sponsored by grant RSF 19-12-00229 in his work on the STELLA code development. N.L. acknowledges funding from grant No. 18-12-00520 from the Russian Scientific Foundation, under support of which analysis of obtained time delays and magnification ratios between images was performed and the Hubble constant was estimated. This research has been supported in part by the RFBR (19-52-50014)-JSPS bilateral program. This work has been supported by the World Premier International Research Center Initiative (WPI), MEXT, Japan, and JSPS KAKENHI grant Nos. JP17K05382 and JP20K04024. We thank the anonymous referee for useful suggestions and remarks that helped improve the paper.

Software: STELLA, emcee Foreman-Mackey et al. (2013), matplotlib (Hunter 2007).

Appendix Fitting Model Light Curves to Observations

Here, we describe our approach of fitting synthetic LCs to observations. As discussed in Section 3, we constructed a set of 185 hydrodynamic SN models to find the optimal model that interprets simultaneously available photometric and spectroscopic observations of SN Refsdal. Namely, we use well-sampled measurements in the F160W, F125W, and F105W bands and H α velocities as constraints. For each SN model, we derive the logarithmic likelihood function (A1):

$$\log L(m^o|m^m, \Theta) = -\frac{1}{2} \sum_{S,t} \left[\frac{(m_S^o(t) - m_S^m(t + \Delta t) - \Delta m)^2}{\sigma_S^2} + \log(2\pi\sigma_S^2) \right], \quad (\text{A1})$$

where $m_S^m(t)$ is the model LC in a given filter S ($S = \text{F160W}$, F125W , or F105W), $m_S^o(t)$ is the observed LC in a filter S sampled at time instances t , and the total uncertainties $\sigma_S^2 = \sigma_o^2 + \sigma_m^2$ are represented with two components, the observational photometric uncertainties σ_o and the model uncertainties σ_m . Summation is done over three HST filters

and time instances at which observations are available. Vector Θ denotes the set of five free parameters—the time shift Δt , the magnitude shift Δm , and the model uncertainties σ_m for F105W, F125W, and F160W filters—which we determine for each SN model by maximizing the log-likelihood (A1). Since STELLA allows one to calculate LCs in multiple bands self-consistently, to match observations we shift all synthetic LCs in brightness by a single value of Δm without adding any filter-related corrections. Unfortunately, the “true” model uncertainties are hard to evaluate. Moreover, STELLA is 1D and makes several simplifying assumptions to numerically treat the radiation hydrodynamics. Thus, the perfect fit of a model to observations does not necessarily lead one to the “true” physical parameters. It is more important that the model captures correctly the general shape of the observed LCs. That is why we artificially introduced the model uncertainties for each band as fitting parameters. Such an approach also allows us to assign (implicitly) different weights to observations in different bands. For example, as can be seen from Table 4, the best-fit model uncertainty for filter F105W is always larger than σ_m for F160W. This is partly due to the fact that data in filter F105W are much sparser and with larger error bars than measurements in F160W.

Having the absolute Δt and Δm of image S1 fixed, we fit the model LCs to images S2, S3, S4, and SX by maximizing the function (A1) with five free parameters: the time delay of a considered image relative to S1, the magnitude shift relative to S1, and the model uncertainties for three considered HST filters.

We use flat priors for all the fit parameters with the following ranges: the absolute time shift for the image S1 $\in (-150, 0)$ days, time shifts for images S2–S4 defined relative to S1 $\in (-70, 70)$ days, all the magnitude shifts $\Delta m \in (-5, 5)$, and the model uncertainties $\sigma_m \in (0, 1)$. The likelihood distributions are sampled using the Markov Chain Monte Carlo ensemble sampling tools from the emcee software package (Foreman-Mackey et al. 2013).

Next, we derive the model evidence (the marginal distributions of the observations D given the SN model M_i averaged over the prior distributions of all the parameters constituting the vector Θ):

$$\pi(D|M_i) = \int_i L(\Theta_i) Pr(\Theta_i). \quad (\text{A2})$$

Table 4
Parameters of the Eight Best-performing SN Models

Model	$\pi(M_i D)$	Δt (days)	Δm	$\sigma_m(\text{F160W})$	$\sigma_m(\text{F125W})$	$\sigma_m(\text{F105W})$	R_0 (R_\odot)	M_{tot} (M_\odot)	$M_{^{56}\text{Ni}}$ (M_\odot)	E_{burst} (E51)
M1	0.711	$-72^{+2.6}_{-2.2}$	$-2.57^{+0.024}_{-0.029}$	$0.11^{+0.03}_{-0.05}$	$0.16^{+0.04}_{-0.05}$	$0.14^{+0.04}_{-0.03}$	50.0	26.3	0.25	5.0
M2	0.165	$-111^{+2.7}_{-2.7}$	$-2.18^{+0.027}_{-0.047}$	$0.10^{+0.05}_{-0.03}$	$0.17^{+0.05}_{-0.05}$	$0.16^{+0.05}_{-0.04}$	50.0	20.6	0.37	3.0
M3	0.088	$-71^{+2.4}_{-2.5}$	$-2.57^{+0.025}_{-0.028}$	$0.12^{+0.03}_{-0.02}$	$0.16^{+0.04}_{-0.03}$	$0.13^{+0.04}_{-0.03}$	50.0	26.0	0.24	5.0
M4	0.0258	$-33^{+0.4}_{-0.4}$	$-3.17^{+0.017}_{-0.017}$	$0.10^{+0.02}_{-0.02}$	$0.17^{+0.04}_{-0.03}$	$0.11^{+0.04}_{-0.03}$	45.0	25.0	0.12	6.0
M5	0.0047	$-109^{+2.8}_{-4.5}$	$-2.58^{+0.018}_{-0.028}$	$0.06^{+0.03}_{-0.02}$	$0.25^{+0.05}_{-0.05}$	$0.31^{+0.07}_{-0.07}$	50.0	26.3	0.24	3.0
M6	0.0022	$-45^{+3.3}_{-2.4}$	$-3.22^{+0.020}_{-0.022}$	$0.09^{+0.02}_{-0.02}$	$0.21^{+0.04}_{-0.03}$	$0.19^{+0.05}_{-0.04}$	40.0	26.0	0.12	5.5
M7	0.0021	$-87^{+3.2}_{-3.7}$	$-2.57^{+0.027}_{-0.062}$	$0.10^{+0.07}_{-0.03}$	$0.19^{+0.05}_{-0.06}$	$0.21^{+0.05}_{-0.06}$	50.0	26.0	0.24	4.0
M8	0.0012	$-108^{+3.3}_{-5.1}$	$-2.59^{+0.020}_{-0.035}$	$0.07^{+0.04}_{-0.02}$	$0.25^{+0.05}_{-0.06}$	$0.31^{+0.07}_{-0.08}$	50.0	26.0	0.24	3.0

Note. Parameters of the best-fit model (with the highest value of $\pi(M_i|D)$ in the first row). Columns (3)–(7) list the best values of fit parameters: the absolute time shift of S1 in days relative to $\text{MJD}_0 = 57,000$, the absolute magnitude shift of S1, and the model uncertainties in three HST passbands. Columns (8)–(11) give information on physical parameters of each SN model, namely, the pre-SN radius, the total mass, the radioactive ^{56}Ni mass, and the explosion energy (in units of 10^{51} erg).

Table 5
Time Delay and Magnification Measurements for SN Refsdal Images S1–S4

Model	$\pi(M_l D)$	MJD _{exp}	MJD _{pk}	Δt_{S2-S1}	Δt_{S3-S1}	Δt_{S4-S1}	μ_{S1}	$\mu_{S2/S1}$	$\mu_{S3/S1}$	$\mu_{S4/S1}$
M1	0.711	56928 ^{+2.57} _{-2.23}	57145 ^{+2.6} _{-2.2}	10.0 ^{+1.93} _{-2.04}	4.2 ^{+2.35} _{-2.34}	30.4 ^{+6.59} _{-8.00}	10.62 ^{+0.285} _{-0.229}	1.14 ^{+0.019} _{-0.019}	1.01 ^{+0.019} _{-0.018}	0.34 ^{+0.015} _{-0.014}
M2	0.165	56889 ^{+2.70} _{-2.79}	57141 ^{+2.7} _{-2.8}	8.7 ^{+2.43} _{-2.45}	4.5 ^{+1.82} _{-1.97}	31.0 ^{+9.28} _{-7.81}	7.43 ^{+0.327} _{-0.176}	1.12 ^{+0.019} _{-0.019}	1.01 ^{+0.015} _{-0.014}	0.35 ^{+0.019} _{-0.015}
M3	0.088	56929 ^{+2.37} _{-2.47}	57138 ^{+2.4} _{-2.5}	11.2 ^{+1.86} _{-2.44}	4.7 ^{+2.62} _{-2.54}	28.7 ^{+6.70} _{-4.62}	10.71 ^{+0.283} _{-0.248}	1.14 ^{+0.020} _{-0.020}	1.01 ^{+0.020} _{-0.019}	0.34 ^{+0.013} _{-0.012}
M4	0.0258	56967 ^{+0.37} _{-0.45}	57134 ^{+0.4} _{-0.4}	0.5 ^{+0.28} _{-0.38}	0.5 ^{+0.28} _{-0.40}	12.2 ^{+1.04} _{-1.91}	18.59 ^{+0.302} _{-0.292}	1.11 ^{+0.018} _{-0.019}	1.01 ^{+0.016} _{-0.016}	0.33 ^{+0.010} _{-0.010}
M5	0.0047	56891 ^{+2.95} _{-5.49}	57150 ^{+3.0} _{-3.5}	9.4 ^{+3.20} _{-3.61}	4.7 ^{+1.85} _{-1.93}	34.0 ^{+10.84} _{-10.04}	10.74 ^{+0.403} _{-0.186}	1.15 ^{+0.024} _{-0.022}	1.03 ^{+0.013} _{-0.013}	0.38 ^{+0.024} _{-0.019}
M6	0.0022	56955 ^{+3.26} _{-2.48}	57166 ^{+3.3} _{-2.5}	12.0 ^{+0.54} _{-0.92}	1.0 ^{+1.38} _{-1.83}	20.5 ^{+3.32} _{-5.66}	19.41 ^{+0.388} _{-0.345}	1.15 ^{+0.019} _{-0.018}	1.00 ^{+0.013} _{-0.013}	0.35 ^{+0.013} _{-0.013}
M7	0.0021	56913 ^{+3.23} _{-3.72}	57152 ^{+3.2} _{-3.7}	10.7 ^{+2.85} _{-3.23}	5.3 ^{+2.62} _{-2.61}	33.1 ^{+7.55} _{-7.27}	10.69 ^{+0.648} _{-0.265}	1.14 ^{+0.022} _{-0.021}	1.02 ^{+0.019} _{-0.017}	0.36 ^{+0.016} _{-0.015}
M8	0.0012	56892 ^{+3.12} _{-4.66}	57145 ^{+3.1} _{-4.7}	8.8 ^{+3.30} _{-3.34}	4.9 ^{+2.26} _{-2.34}	32.4 ^{+11.35} _{-10.21}	10.81 ^{+0.344} _{-0.192}	1.15 ^{+0.023} _{-0.022}	1.03 ^{+0.014} _{-0.014}	0.37 ^{+0.024} _{-0.018}
BMA	...	56922 ^{+18.6} _{-18.6}	57144 ⁺¹⁰ ₋₁₀	9.5 ^{+2.6} _{-2.7}	4.2 ^{+2.3} _{-2.3}	30 ^{+7.8} _{-8.2}	10.2 ^{+1.9} _{-1.6}	1.14 ^{+0.021} _{-0.020}	1.01 ^{+0.019} _{-0.018}	0.35 ^{+0.016} _{-0.015}

Note. Columns (3) and (4) show the modified Julian dates of the explosion and the peak, correspondingly. Columns (5)–(7) provide the time delays (in days) relative to S1. Column (8) lists the absolute magnifications for S1, while Columns (9)–(11) give magnifications of images S2–S4 relative to S1.

Then, we define the posterior probability of each SN model given observations as

$$\pi(M_l|D) = \frac{\pi(D|M_l)\pi(M_l)}{\sum_m \pi(D|M_m)\pi(M_m)}, \quad (\text{A3})$$

where we sum up over all 185 SN models in the denominator to ensure that the cumulative posterior probability over all models equals unity. Obtained posterior probabilities $\pi(M_l|D)$ can be used as a straightforward model selection criterion (Hoeting et al. 1999), with the most likely model having the highest value of $\pi(M_l|D)$.

For each SN model in our set, we evaluate $\pi(M_l|D)$ by comparing the synthetic LCs with observations for SN Refsdal images S1–S4 in F105W, F125W, and F160W passbands. As a result, for each SN model we obtain $\pi(M_l|D)$ and the best-fitting parameters: the absolute time shift of image S1, i.e., modified Julian date of the explosion (MJD_{exp}), and the absolute magnification of S1 (both of which are actually nuisance parameters), the time shifts of images S2–S4 relative to S1, and magnification ratios. Table 4 lists the best-fit parameters for S1 (the absolute time shift Δt , the absolute magnitude shift Δm , and the model uncertainties σ_m for F105W, F125W, and F160W filters), as well as the basic SN model characteristics for eight best-performing models. Figure 8 plots their synthetic LCs with the observations for SN Refsdal images S1–S4 shifted by the corresponding Δt and Δm . Note that the best-fit absolute magnifications of S1 $\mu = 10^{-\Delta m/2.5} \simeq 7.5 - 20$ for SN models in Table 4 are in approximate agreement with absolute magnifications predicted by lens models (Oguri 2015; Kawamata et al. 2016; Sharon & Johnson 2015; Jauzac et al. 2016; Grillo et al. 2016). This is not a result of fine-tuning since for Δm determination we used a flat prior in a wide range of values $\Delta m \in (-5, 5)$. Table 5 shows relative time delays for images S2–S4 in days, magnification ratios, and the explosion and peak MJDs. Despite the fact that for the top three SN models (the first

three rows in Table 5) the explosion dates (or the absolute time shift in Table 4) vary noticeably, the resulting relative time delays are not that different. A similar conclusion can be made about magnifications. The absolute magnification varies at most by a factor of ~ 2.5 , while the relative magnifications (Columns (9)–(11) of Table 5) show variations by several percent only. Table 4 also provides values of $\pi(M_l|D)$ for each model that reflect quality of fit to the data. The best-fit model M1 (see Table 4) significantly outperforms all the others (which is not surprising since it was our goal to construct the SN model that matches best available SN Refsdal observations). For the best-fit model, Figure 7 plots 2D and 1D probability distributions of each of the five fit parameters.

We compute a weighted average and an uncertainty of parameters of interest Θ across the explored set of SN models M_l using the BMA approach (Hoeting et al. 1999):

$$E[\Theta] = \sum_l \pi(M_l|D) \Theta_l \quad (\text{A4})$$

$$\text{Var}[\Theta] = \left| \pi(M_l|D) (\text{Var}(\Theta_l) + \Theta^2) - E[\Theta]^2 \right|. \quad (\text{A5})$$

The same procedure of finding the best-fit time and magnitudes shifts is applied to SN Refsdal image SX. We use flat priors on free parameters: the absolute magnitude shift $\Delta m \in (-2, 0)$, model uncertainties $\sigma_m \in (0, 1)$. The time delay relative to S1 is varied within the range that depends on an SN model and is defined from the following two conditions: (i) in 2016 January SX showed brightening (Kelly et al. 2016), and (ii) SX appeared no earlier than on 2005 October 30 (Kelly et al. 2016).

The best-performing models are shown in Figure 9. The marginal distributions of fit parameters for the best-fit model M1 are illustrated in Figure 10. The final time delay and magnification ratio estimates for SX (relative to S1) are obtained again via BMA and provided in Section 4.2.

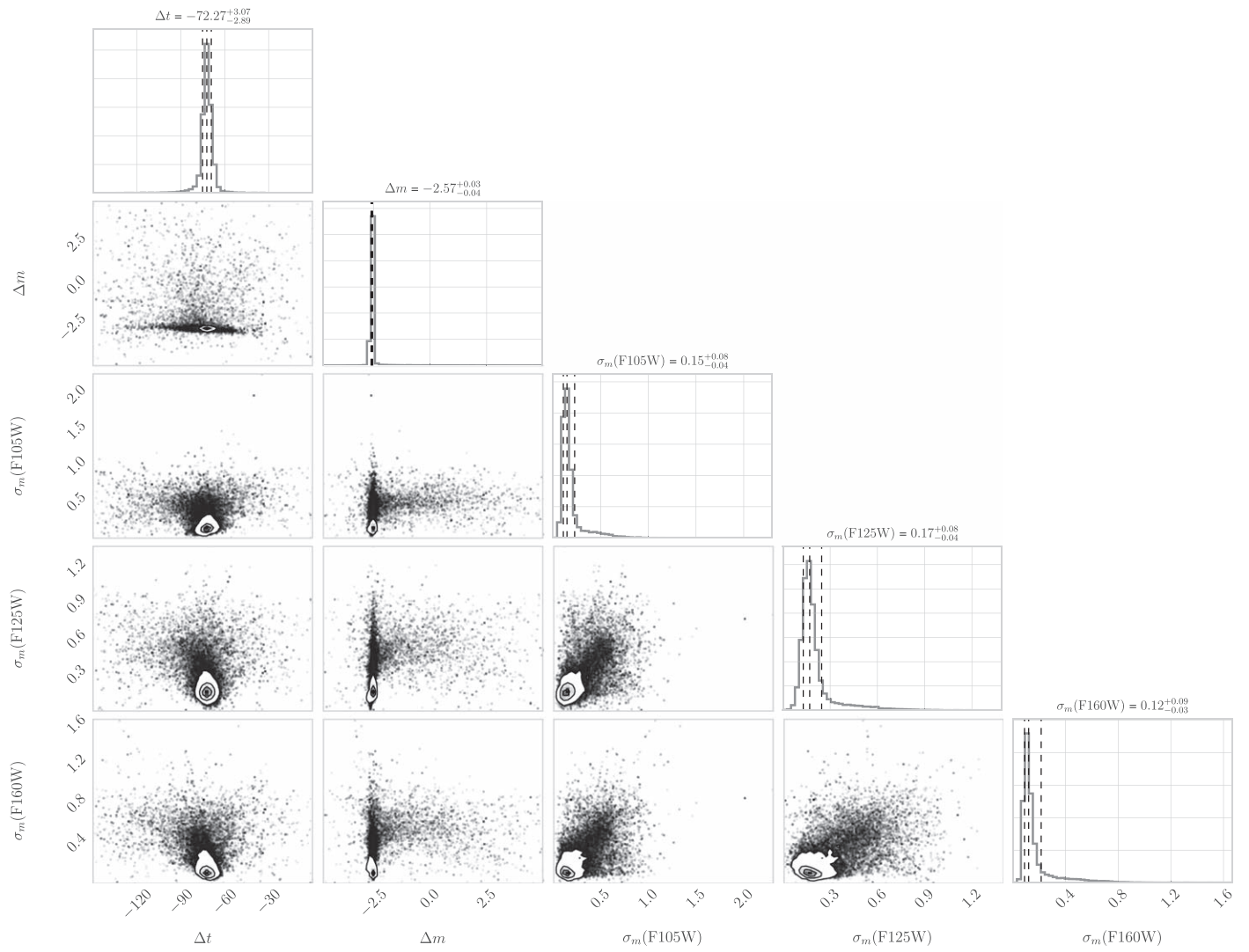


Figure 7. MCMC corner plot for the best-fit model M1 showing 1D and 2D marginalized probability contours for each of the five fit parameters (the absolute time shift and the absolute magnitude shift of image S1, and the model uncertainties in three passbands). The histograms on the diagonal also include the positions of the 16th, 50th, and 84th percentiles.

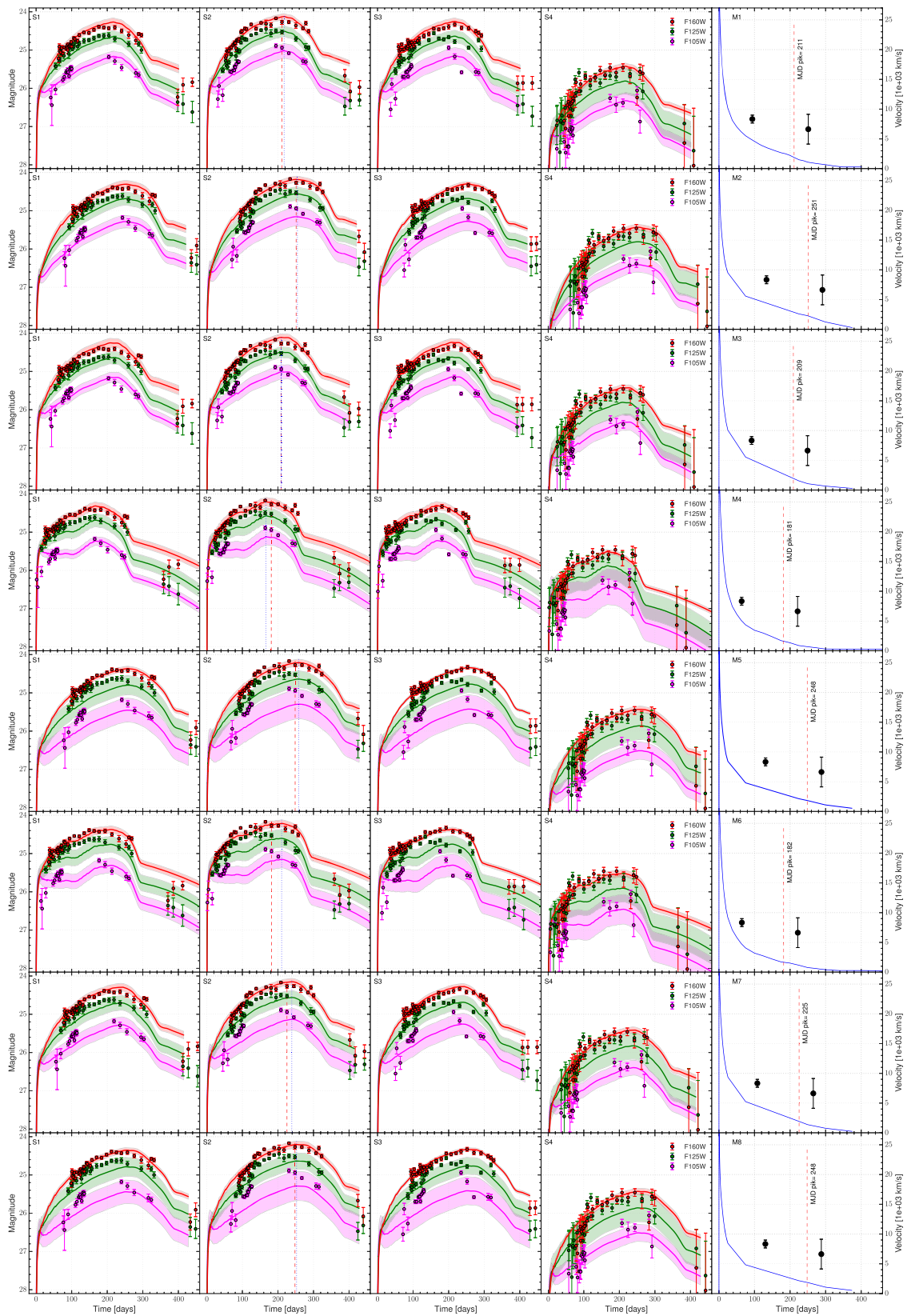


Figure 8. LCs and the photosphere velocity evolution of the best-performing SN models listed in Table 4. The best-fit model M1 is shown in the first row, M2 is in the second, ..., M8 is in the eighth row. In each row, the first four panels show the observed and model LCs for SN Refsdal images S1–S4 (from left to right). Shaded areas indicate the model uncertainties in each passband. The rightmost panel in each row plots the model photospheric velocity evolution in comparison with H α velocity measurements from Kelly et al. (2016). As expected, H α velocities are systematically higher than the photospheric velocities. The vertical dashed line shows the date of peak brightness of a model LC in F160W passband.

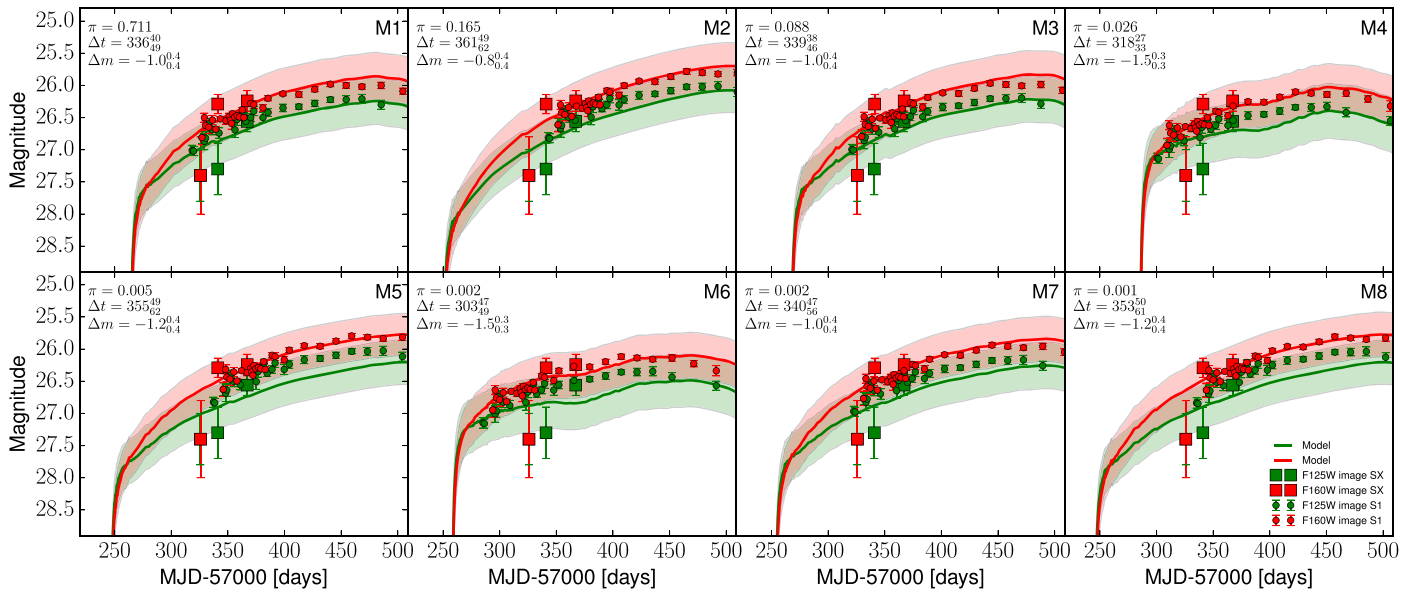


Figure 9. Model LCs of eight best-performing models fitted to the SX data (shown as squares). For comparison, S1 data are overlotted as circles.

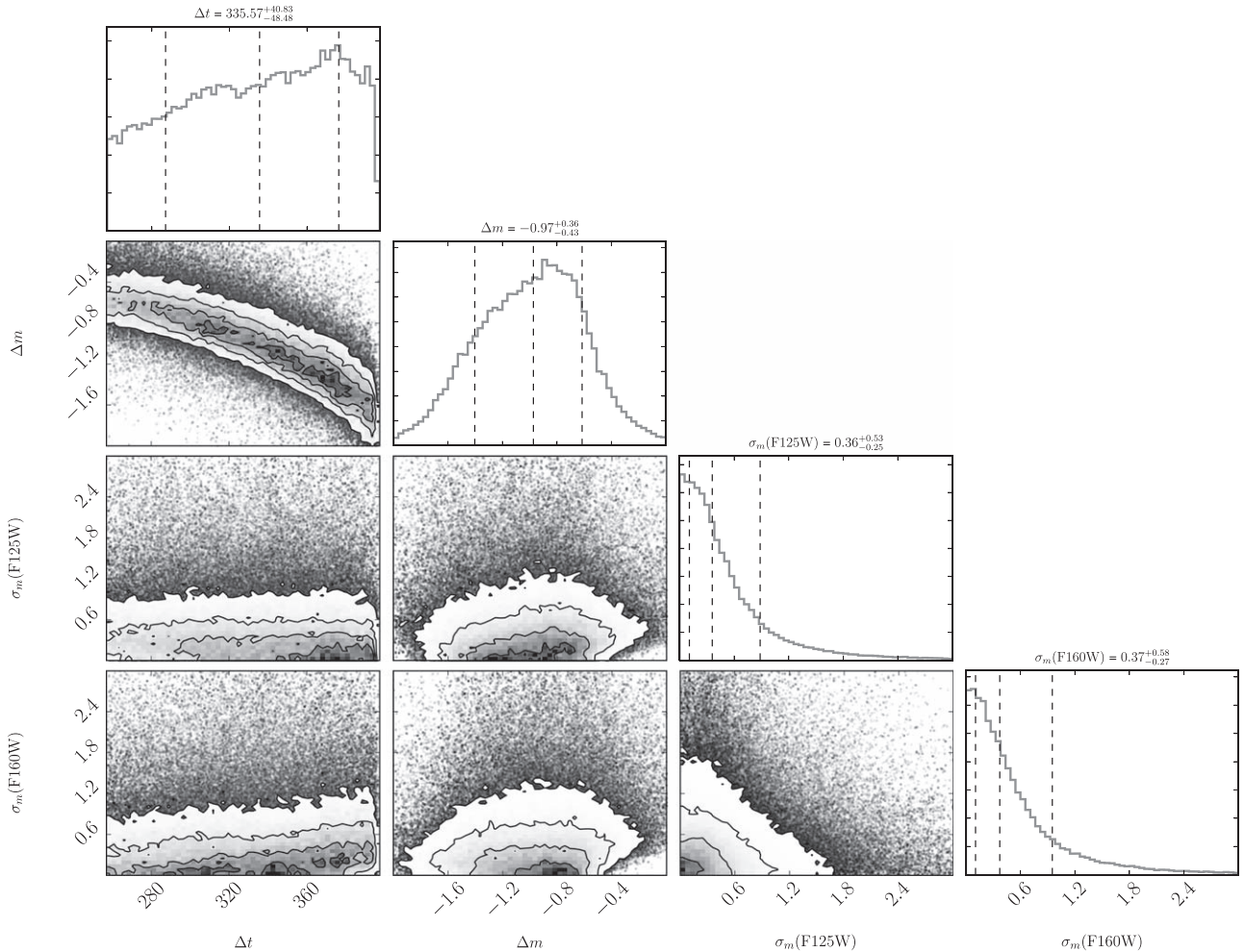






Figure 10. MCMC corner plot for the best-fit model M1 showing marginal distributions for the following fit parameters: the SX-S1 time delay, the absolute magnitude shift for SX (which can be related to the magnification ratio as $\mu_{\text{SX}/\text{S1}} = 10^{-\Delta m/2.5}/\mu_{\text{S1}}$, where $\mu_{\text{S1}} = 10.62$ is the absolute magnification for S1), and the model uncertainties in F125W and F160W filters. Dashed vertical lines in the histograms on the diagonal mark the positions of the 16th, 50th, and 84th percentiles.

ORCID iDs

Petr Baklanov  <https://orcid.org/0000-0002-5920-1478>
 Natalia Lyskova  <https://orcid.org/0000-0003-4917-7803>
 Sergei Blinnikov  <https://orcid.org/0000-0002-5726-538X>
 Ken'ichi Nomoto  <https://orcid.org/0000-0001-9553-0685>

References

- Baklanov, P. V., Blinnikov, S. I., & Pavlyuk, N. N. 2005, *AstL*, **31**, 429
 Baklanov, P. V., Blinnikov, S. I., Potashov, M. S., & Dolgov, A. D. 2013, *JETPL*, **98**, 432
 Baklanov, P. V., Sorokina, E. I., & Blinnikov, S. I. 2015, *AstL*, **41**, 95
 Baron, E., Nugent, P. E., Branch, D., & Hauschildt, P. H. 2004, *ApJL*, **616**, L91
 Bartunov, O. S., Blinnikov, S., Levakhina, L. V., & Nadezhin, D. 1987, *SvAL*, **13**, 313
 Birrer, S., Amara, A., & Refregier, A. 2016, *JCAP*, **2016**, 020
 Blanco, W. M., Gregory, B., Hamuy, M., et al. 1987, *ApJ*, **320**, 589
 Blinnikov, S., & Sorokina, E. 2004, *Ap&SS*, **290**, 13
 Blinnikov, S. I., Lundqvist, P., Bartunov, O. S., Nomoto, K., & Iwamoto, K. 2000, *ApJ*, **532**, 1132
 Blinnikov, S. I., Röpke, F. K., Sorokina, E. I., et al. 2006, *A&A*, **453**, 229
 Chen, K.-J., Woosley, S. E., & Whalen, D. J. 2020, *ApJ*, **893**, 99
 Cooke, J., Sullivan, M., Gal-Yam, A., et al. 2012, *Natur*, **491**, 228
 Dobler, G., Fassnacht, C. D., Treu, T., et al. 2015, *ApJ*, **799**, 168
 Dobler, G., & Keeton, C. R. 2006, *ApJ*, **653**, 1391
 Eastman, R. G., & Pinto, P. A. 1993, *ApJ*, **412**, 731
 Eigenbrod, A., Courbin, F., Vuissoz, C., et al. 2005, *A&A*, **436**, 25
 Foreman-Mackey, D., Hogg, D. W., Lang, D., & Goodman, J. 2013, *PASP*, **125**, 306
 Gall, E. E. E., Kotak, R., Leibundgut, B., et al. 2018, *A&A*, **611**, A25
 Goldstein, D. A., Nugent, P. E., Kasen, D. N., & Collett, T. E. 2018, *ApJ*, **855**, 22
 Goobar, A., Amanullah, R., Kulkarni, S. R., et al. 2017, *Sci*, **356**, 291
 Grillo, C., Karman, W., Suyu, S. H., et al. 2016, *ApJ*, **822**, 78
 Grillo, C., Rosati, P., Suyu, S. H., et al. 2018, *ApJ*, **860**, 94
 Grillo, C., Rosati, P., Suyu, S. H., et al. 2020, *ApJ*, **898**, 87
 Hillebrandt, W., Höflich, P., Truran, J. W., & Weiss, A. 1987, *Natur*, **327**, 597
 Hoeting, J. A., Madigan, D., Raftery, A. E., & Volinsky, C. T. 1999, *StaSc*, **14**, 382
 Huber, S., Suyu, S. H., Noebauer, U. M., et al. 2019, *A&A*, **631**, A161
 Hunter, J. D. 2007, *CSE*, **9**, 90
 Jauzac, M., Richard, J., Limousin, M., et al. 2016, *MNRAS*, **457**, 2029
 Kawamata, R., Oguri, M., Ishigaki, M., Shimasaku, K., & Ouchi, M. 2016, *ApJ*, **819**, 114
 Kelly, P. L., Brammer, G., Selsing, J., et al. 2016, *ApJ*, **831**, 205
 Kelly, P. L., Rodney, S. A., Treu, T., et al. 2015, *Sci*, **347**, 1123
 Kelly, P. L., Rodney, S. A., Treu, T., et al. 2016, *ApJL*, **819**, L8
 Kirshner, R. P., & Kwan, J. 1974, *ApJ*, **193**, 27
 Kochanek, C. S. 2002, *ApJ*, **578**, 25
 Kumagai, S., Shigeyama, T., Nomoto, K., et al. 1989, *ApJ*, **345**, 412
 Larchenkova, T. I., Lutovinov, A. A., & Lyskova, N. S. 2011, *AstL*, **37**, 233
 Linder, E. V. 2011, *PhRvD*, **84**, 123529
 Lotz, J. M., Koekemoer, A., Coe, D., et al. 2017, *ApJ*, **837**, 97
 McCray, R., & Fransson, C. 2016, *ARA&A*, **54**, 19
 Menon, A., Utrobin, V., & Heger, A. 2019, *MNRAS*, **482**, 438
 Müller, T., Prieto, J. L., Pejcha, O., & Clocchiatti, A. 2017, *ApJ*, **841**, 127
 Nadyozhin, D. 2003, *MNRAS*, **346**, 97
 Nomoto, K., & Hashimoto, M. 1988, *PhR*, **163**, 13
 Nugent, P., & Hamuy, M. 2017, in *Handbook of Supernovae*, ed. A. W. Alsabti & P. Murdin (Berlin: Springer), 2671
 Oguri, M. 2015, *MNRAS*, **449**, L86
 Oguri, M., & Kawano, Y. 2003, *MNRAS*, **338**, L25
 Perlmutter, S., Aldering, G., Goldhaber, G., et al. 1999, *ApJ*, **517**, 565
 Pierel, J. D. R., & Rodney, S. 2019, *ApJ*, **876**, 107
 Potashov, M., Blinnikov, S. I., Baklanov, P. V., & Dolgov, A. 2013, *MNRAS*, **431**, L98
 Refsdal, S. 1964, *MNRAS*, **128**, 307
 Riehm, T., Mörtzell, E., Goobar, A., et al. 2011, *A&A*, **536**, A94
 Riess, A. G., Filippenko, A. V., Challis, P., et al. 1998, *AJ*, **116**, 1009
 Rodney, S. A., Strolger, L. G., Kelly, P. L., et al. 2016, *ApJ*, **820**, 50
 Sahu, D. K., Tanaka, M., Anupama, G. C., et al. 2008, *ApJ*, **680**, 580
 Saio, H., Nomoto, K., & Kato, M. 1988, *Natur*, **334**, 508
 Sharon, K., & Johnson, T. L. 2015, *ApJL*, **800**, L26
 Shigeyama, T., & Nomoto, K. 1990, *ApJ*, **360**, 242
 Sorokina, E., Blinnikov, S., Nomoto, K., Quimby, R., & Tolstov, A. 2016, *ApJ*, **829**, 17
 Stanishev, V., Goobar, A., Paech, K., et al. 2009, *A&A*, **507**, 61
 Sukhbold, T., Ertl, T., Woosley, S. E., Brown, J. M., & Janka, H.-T. 2016, *ApJ*, **821**, 38
 Suyu, S. H., Bonvin, V., Courbin, F., et al. 2017, *MNRAS*, **468**, 2590
 Suyu, S. H., Huber, S., Cañameras, R., et al. 2020, *A&A*, **644**, A162
 Taddia, F., Stritzinger, M. D., Sollerman, J., et al. 2012, *A&A*, **537**, A140
 Tewes, M., Courbin, F., Meylan, G., et al. 2013, *A&A*, **556**, A22
 Tominaga, N., Morokuma, T., Blinnikov, S. I., et al. 2011, *ApJS*, **193**, 20
 Treu, T., Brammer, G., Diego, J. M., et al. 2016, *ApJ*, **817**, 60
 Tsvetkov, D. Y., Baklanov, P. V., Potashov, M. S., et al. 2019, *MNRAS*, **487**, 3001
 Utrobin, V. P. 2005, *AstL*, **31**, 806
 Utrobin, V. P., & Chugai, N. N. 2011, *A&A*, **532**, A100
 Vega-Ferrero, J., Diego, J. M., Miranda, V., & Bernstein, G. M. 2018, *ApJL*, **853**, L31
 Wong, K. C., Suyu, S. H., Chen, G. C.-F., et al. 2020, *MNRAS*, **498**, 1420
 Woosley, S. E., Blinnikov, S., & Heger, A. 2007a, *Natur*, **450**, 390
 Woosley, S. E., Kasen, D., Blinnikov, S., & Sorokina, E. 2007b, *ApJ*, **662**, 487
 Xu, D., Sluse, D., Schneider, P., et al. 2016, *MNRAS*, **456**, 739